



RESEARCH LETTER

10.1002/2016GL071190

Key Points:

- ENSO's complex temporal and spatial diversities can be well captured when combining equatorial and off-equatorial SSTAs to a new metric
- This metric captures a robust year-round ENSO/monsoon relationship and the Yangtze River basin summer flooding events
- The ENSO complexity captured by the metric can be predicted several months in advance, thereby providing monsoon predictability

Supporting Information:

- Supporting Information S1

Correspondence to:

F.-F. Jin,
jff@hawaii.edu

Citation:

Zhang, W., F.-F. Jin, M. F. Stuecker, A. T. Wittenberg, A. Timmermann, H.-L. Ren, J.-S. Kug, W. Cai, and M. Cane (2016), Unraveling El Niño's impact on the East Asian Monsoon and Yangtze River summer flooding, *Geophys. Res. Lett.*, *43*, 11,375–11,382, doi:10.1002/2016GL071190.

Received 12 SEP 2016

Accepted 22 OCT 2016

Accepted article online 26 OCT 2016

Published online 15 NOV 2016

Unraveling El Niño's impact on the East Asian Monsoon and Yangtze River summer flooding

Wenjun Zhang¹, Fei-Fei Jin^{2,3}, Malte F. Stuecker², Andrew T. Wittenberg⁴, Axel Timmermann⁵, Hong-Li Ren³, Jong-Seong Kug⁶, Wenju Cai⁷, and Mark Cane⁸

¹Key Laboratory of Meteorological Disaster of Ministry of Education, ILCEC/CIC-FEMD, Nanjing University of Information Science and Technology, Nanjing, China, ²Department of Atmospheric Sciences, SOEST, University of Hawai'i at Mānoa, Honolulu, Hawaii, USA, ³Laboratory for Climate Studies, National Climate Center, China Meteorological Administration, Beijing, China, ⁴Geophysical Fluid Dynamics Laboratory, National Oceanic and Atmospheric Administration, Princeton, New Jersey, USA, ⁵IPRC, SOEST, University of Hawai'i at Mānoa, Honolulu, Hawaii, USA, ⁶School of Environmental Science and Engineering, Pohang University of Science and Technology, Pohang, South Korea, ⁷CSIRO Oceans and Atmosphere, Victoria, Australia, ⁸Lamont-Doherty Earth Observatory, Columbia University, Palisades, NY, USA

Abstract Strong El Niño events are followed by massive summer monsoon flooding over the Yangtze River basin (YRB), home to about a third of the population in China. Although the El Niño–Southern Oscillation (ENSO) provides the main source of seasonal climate predictability for many parts of the Earth, the mechanisms of its connection to the East Asian monsoon remain largely elusive. For instance, the traditional Niño3.4 ENSO index only captures precipitation anomalies over East Asia in boreal winter but not during the summer. Here we show that there exists a robust year-round and predictable relationship between ENSO and the Asian monsoon. This connection is revealed by combining equatorial (Niño3.4) and off-equatorial Pacific sea surface temperature anomalies (Niño-A index) into a new metric that captures ENSO's various aspects, such as its interaction with the annual cycle and its different flavors. This extended view of ENSO complexity improves predictability of YRB summer flooding events.

1. Introduction

The El Niño–Southern Oscillation (ENSO), which originates in the equatorial Pacific, is the dominant mode of interannual climate variability (Figures 1a and 1b) and has pronounced global climate impacts [Latif *et al.*, 1998; Neelin *et al.*, 1998; Trenberth *et al.*, 1998; Wallace *et al.*, 1998; McPhaden *et al.*, 2006]. For instance, destructive Asian summer monsoon flooding events occurred in the Yangtze River basin (YRB), the crucial water catchment in China, following the peak of the two major El Niño events in 1982/1983 and 1997/1998 (Figures 2a and 2d). The 2016 massive summer flooding in this area is further testimony to a linkage between Pacific sea surface temperatures (SST) and Asian rainfall anomalies (Figures 2a and 2d). However, the widely used ENSO SST index, commonly referred to as the Niño3.4 index (defined as the SST anomalies averaged over the region 5°S–5°N and 120°W–170°W; Figures 1a and 1b), fails to capture this ENSO impact on the East Asian Monsoon system (Figures 2b and 2e).

Recent studies showed that nonlinear interactions between ENSO and the background annual cycle result in a conspicuous deterministic spatial and temporal expansion of ENSO's signal via the generation of an ENSO/annual cycle combination mode (C-mode) [Stuecker *et al.*, 2013], characterized by near-annual combination tone periods at ~10 and ~15 months and distinct meridionally asymmetric patterns in both atmospheric variables [Stuecker *et al.*, 2013, 2015a, 2015b] and SST anomalies (Figures 1c and 1d). In addition, recent observations show that ENSO exhibits pronounced diversity ("flavors") in its zonal SST structures and corresponding impacts [Ashok *et al.*, 2007; Kug *et al.*, 2009; Kao and Yu, 2009; Yeh *et al.*, 2009; Ren and Jin, 2011; Takahashi *et al.*, 2011; Capotondi *et al.*, 2015]. Two main El Niño flavors are distinguished, an eastern Pacific type (EP-El Niño) and a central Pacific type (CP-El Niño), which is also referred to as El Niño Modoki [Ashok *et al.*, 2007].

Our understanding of ENSO's complex temporal and spatial diversities is still in its infancy. This uncertainty is also reflected by the number of hypotheses that explain the widely varying ENSO-monsoon relationship [Webster *et al.*, 1998; Wang *et al.*, 2000; Yang *et al.*, 2007; Xie *et al.*, 2009, 2016; Stuecker *et al.*, 2015a; Zhang *et al.*, 2016]. Importantly, the Niño3.4 index fails to capture ENSO's spatial degrees of freedom as well as its full seasonal dependence. Additional indices that are designed to describe the zonal asymmetry of ENSO's

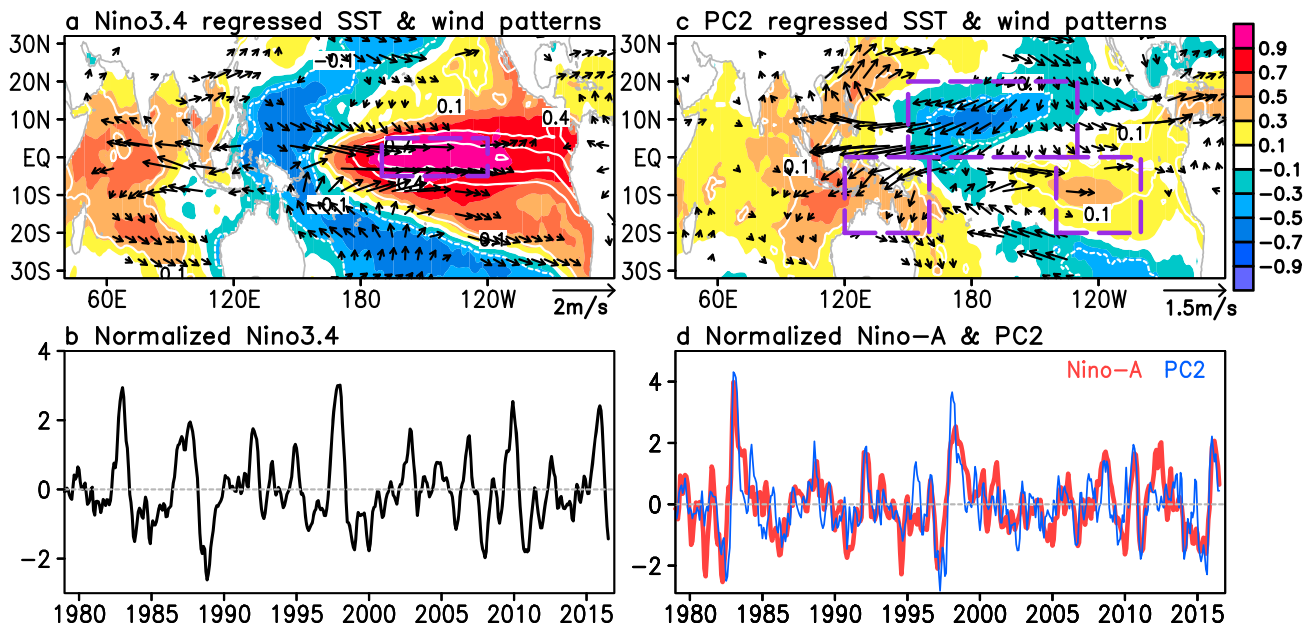


Figure 1. ENSO SST and wind variability. (a) SST (contours with interval 0.3°C and shading for correlation coefficient) and 850 hPa wind (vector in m/s, above the 95% confidence level) anomalies regressed onto the Niño-3.4 index (SST anomalies averaged in purple box region). (b) Normalized Niño-3.4 index. (c) SST and 850 hPa wind anomalies (as in Figure 1a) regressed onto the second principal component (PC2) of the surface wind anomalies over the equatorial Pacific (10°S–10°N, 110°E–90°W). Contour interval is 0.1°C. (d) Normalized PC2 (blue) and Niño-A index (red) as defined in the text based on the SST anomalies in the regions highlighted in the purple boxes in Figure 1c.

SST anomalies for its different flavors [Ashok et al., 2007; Kao and Yu, 2009; Ren and Jin, 2011; Takahashi et al., 2011] do not account for the temporal and spatial expansion of ENSO arising from its nonlinear interaction with the annual cycle. In this study we demonstrate that ENSO-associated climate impacts, such as postpeak El Niño boreal summer extreme flooding events in the YRB, can be quantified and predicted when considering these aspects of ENSO complexity in a unified framework.

2. Results

The ENSO C-mode wind pattern [McGregor et al., 2012; Stuecker et al., 2013], which includes the anomalous low-level Western North Pacific (WNP) anticyclone (Figure 1c), generates a meridionally asymmetric SST anomaly pattern via heat flux forcing [Stuecker et al., 2015a]. Thus, this SST anomaly pattern (Figure S1 in the supporting information) captures the delayed remote effects of equatorial ENSO SST forcing on the regions outside the equatorial eastern Pacific (see section 4). We utilize this forced SST anomaly pattern (Figure S1) to derive a new Niño-Asymmetry SST index (referred to hereafter as Niño-A) to capture two important aspects of ENSO complexity: the imprints of the meridionally asymmetric ENSO C-mode and the zonal SST asymmetries associated with the different ENSO flavors. By construction the Niño-A and Niño-3.4 indices and their corresponding patterns are largely orthogonal to each other (see section 4 and refer to Figures 1, S1, and S2). The Niño-A index is defined as

$$\text{Niño} - A = 0.5[\text{SSTA}]_{\text{SW}} + 0.5[\text{SSTA}]_{\text{SE}} - [\text{SSTA}]_{\text{NC}}, \quad (1)$$

where the brackets represent the area-averaged SST anomalies over the regions SW (0°S–20°S, 120°E–160°E), SE (0°S–20°S, 100°W–140°W), and NC (0°N–20°N, 150°E–130°W).

The Niño-A-associated SST anomaly pattern (Figure S1a) exhibits a very similar structure to the forced C-mode SST pattern (Figures 1c and S1b), with negative SST anomalies over the northern-central (NC) tropical Pacific and positive SST anomalies over the southwestern (SW) and southeastern (SE) tropical Pacific. The Niño-A index also displays some similarity with the El Niño Modoki index (EMI) ($r = -0.58$; Table S1 and Figures S2 in the supporting information) although pronounced differences are evident in their spatial and spectral characteristics (Figure S3). The differences can be explained because the EMI index highlights the

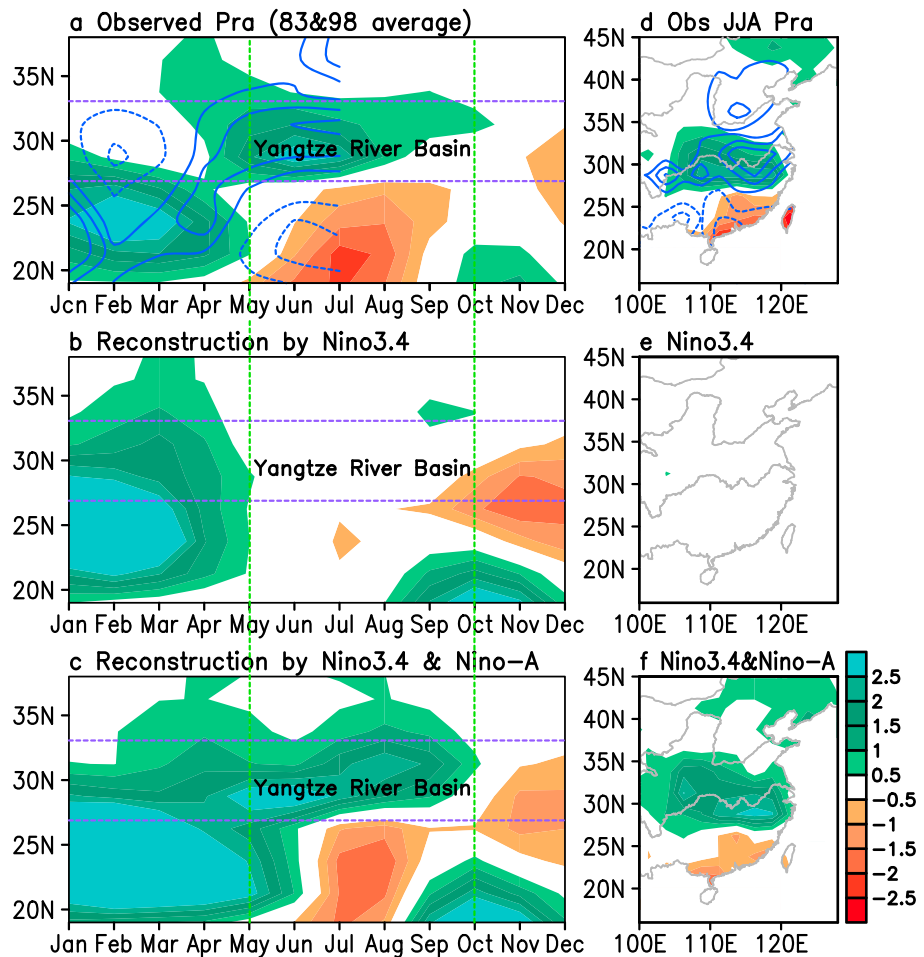


Figure 2. El Niño’s impact on East China precipitation. (a) Observed 2 year (1983 and 1998) average precipitation anomalies (shading, mm/d) over East China (110°E–120°E), and the 2016 precipitation anomalies until July (contour interval 1 mm/d). (b) Reconstruction of precipitation anomalies for the 1983 and 1998 average (shading, mm/d) using linear regression with Niño3.4 index based on the data period of 1979–2015. (c) Same as Figure 2b but using both Niño3.4 and Niño-A for the reconstruction. (d) Observed June–July–August (JJA) precipitation anomalies for the 1983 and 1998 average (shading, mm/d) and June 2016 (contour interval 1 mm/d). (e) Reconstruction for the 1983 and 1998 average JJA precipitation anomalies using linear regression with Niño3.4. (f) Same as Figure 2e but using both Niño3.4 and Niño-A for the reconstruction.

zonal SST anomaly asymmetry at the equator (Figure S3) and it is strongly related to different indices for CP-El Niño events [Ashok et al., 2007; Kao and Yu, 2009; Ren and Jin, 2011; Takahashi et al., 2011]. In contrast, the Niño-A index captures in addition the meridional SST anomaly asymmetry (Figures 1c and S1), as well as the higher frequency C-mode variability characterized by spectral peaks at combination tone periods of ~10 and ~15 months (Figure S3c). Thus, the Niño-A index comprises variability associated with both the C-mode and CP-El Niño events as indicated by their respective correlations (Figure S2 and section 4).

The benefit of using the two-index metric of Niño3.4 and Niño-A becomes apparent when comparing its time evolution with indices of the East Asian Monsoon. El Niño events usually grow in boreal spring and summer, reach their peak phase in boreal winter, and terminate in the following spring and summer seasons (Figure S4a). In contrast, the Niño-A index displays a rapid phase reversal during boreal fall, similar to the C-mode evolution (wind PC2). In addition, it comprises the main feature of the decaying year boreal spring and summer development of Indian Ocean (IO)-Pacific SST anomalies due to persistence owing to the contributions from WNP local air-sea interactions [Wang et al., 2000] and the IO capacitor [Xie et al., 2009; Xie et al., 2016]. The seasonal reversal [Stuecker et al., 2015a] of the anomalous Western Pacific Subtropical High (WPSH), which is closely related to East Asian Summer Monsoon (EASM) anomalies [Wang et al., 2013], is very well captured by the simultaneous Niño-A index (Figures S4b–S4d). The ENSO C-mode

surface wind anomalies induce an ocean mixed layer response via anomalous heat fluxes [e.g., Klein *et al.*, 1999] and thereby generate the Niño-A associated SST anomalies in the off-equatorial Pacific. Hence, it is the memory effect of the ocean mixed layer that allows the C-mode response to persist to the boreal summer season [Stuecker *et al.*, 2015a], thus giving rise to the observed EASM anomalies. Therefore, the Niño-A index comprises the compounding impacts of ENSO on the EASM due to processes involving nonlinear ENSO/annual cycle interactions via C-mode dynamics (characterized by the meridional asymmetric SST anomalies) for the fast-paced seasonal-reversals and its further amplification and persistence by WNP local air-sea interactions and the IO capacitor mechanisms [Stuecker *et al.*, 2015a].

To further illustrate the value of this extended view of ENSO, we demonstrate the separation of the nine observed El Niño events into two types in the two-dimensional Niño3.4-Niño-A state space (Figure S5a). Five events (1982/1983, 1986/1987, 1991/1992, 1997/1998, and 2015/2016), characterized by relatively high positive Niño-A values, exhibit a classic EP-El Niño SST anomaly pattern (Figure S5b). The other five events (1994/1995, 2002/2003, 2004/2005, 2006/2007, and 2009/2010) exhibit negative Niño-A values and feature a so-called CP-El Niño SST anomaly pattern (Figure S5c). Therefore, the Niño-A index also serves as an effective indicator for differentiating El Niño flavors.

When represented only by Niño3.4, the instantaneous correlation between ENSO and the WPSH index is strong only from December to April (Figure S6a). This relationship breaks down in boreal summer. In contrast, a correlation between Niño-A and WPSH during this season is evident (Figure S6a). Therefore, we are able to establish a significant year-round relationship between ENSO and the East Asian Monsoon circulation with our two-index ENSO metric (Figure S6a). In fact, adding other tropical SST anomaly indices to this regression does not improve the correlation significantly any further (Figure S6b).

Similarly, the Niño3.4 and Niño-A indices together explain a significant portion of precipitation variance throughout the year, especially over the YRB during boreal summer, whereas the Niño3.4 index alone only explains the precipitation variability over southern China (south of 30°N) during boreal winter (not shown). Interestingly, the improvement of the explained precipitation (not shown) displays a well-known northward migration following the seasonal march of precipitation [Tao and Chen, 1987], suggesting that the ENSO-induced monsoon onset variability is also captured by the Niño-A index (see also Figures 2a and 2c). During El Niño years, the June-July-August (JJA) Niño-A index correlates well with the precipitation in the YRB ($r=0.77$). Thus, while we are not able to reconstruct the JJA YRB precipitation by using only Niño3.4 (Figure 3b), we are able to do so if we include Niño-A in the reconstruction (Figure 3c). Therefore, by combining Niño3.4 and Niño-A, a year-round relationship between ENSO and Yangtze River basin precipitation can be established (Figure 3a). Naturally, we are only able to recover the ENSO-associated variability. The monsoon precipitation also exhibits large unforced internal variability, which for instance becomes evident when comparing the JJA YRB precipitation anomalies in non-El Niño years (black dots) with those during El Niño years (colored dots) (Figures 3b and 3c).

In particular, our two-index metric captures the YRB flooding in boreal summer following the strong 1982/1983 and 1997/1998 El Niño events (Figures 2c and 2f), which is also seen for the 2016 summer situation (Figures 2a and 2d). In fact, already during March-April-May (2016) above normal precipitation was observed in southern China (exhibiting a similar pattern as in 1983 and 1998), in good agreement with a reconstruction from the two Niño indices (Figure S7). Following the evolution of these indices into summer 2016 using persistence forecasts, we expected an additional increase in summer precipitation in the Yangtze River basin, which was confirmed by the actual summer 2016 observations (Figures 3d and 3e).

3. Discussion

Our extended view of ENSO is not only effective in capturing ENSO's complexity and its important climate impacts but it also provides a way of quantifying the predictability of ENSO complexity. Unlike the Niño3.4 index that has a well-known spring persistence barrier (Figure 4a), the Niño-A index has no apparent spring barrier; instead, its persistence barrier is shifted toward boreal fall (Figure 4b). Despite these persistence barriers, the predictive skill of the Niño-A index is comparable with that of the Niño3.4 index, as inferred from hindcast experiments of five dynamical models, which participated in the ENSEMBLES seasonal forecasting experiments [Weisheimer *et al.*, 2009]. The Niño3.4 and Niño-A indices can both be predicted several months in advance (Figures 4c and 4d). However, the Niño-A's hindcast skill is slightly lower than that for Niño3.4,

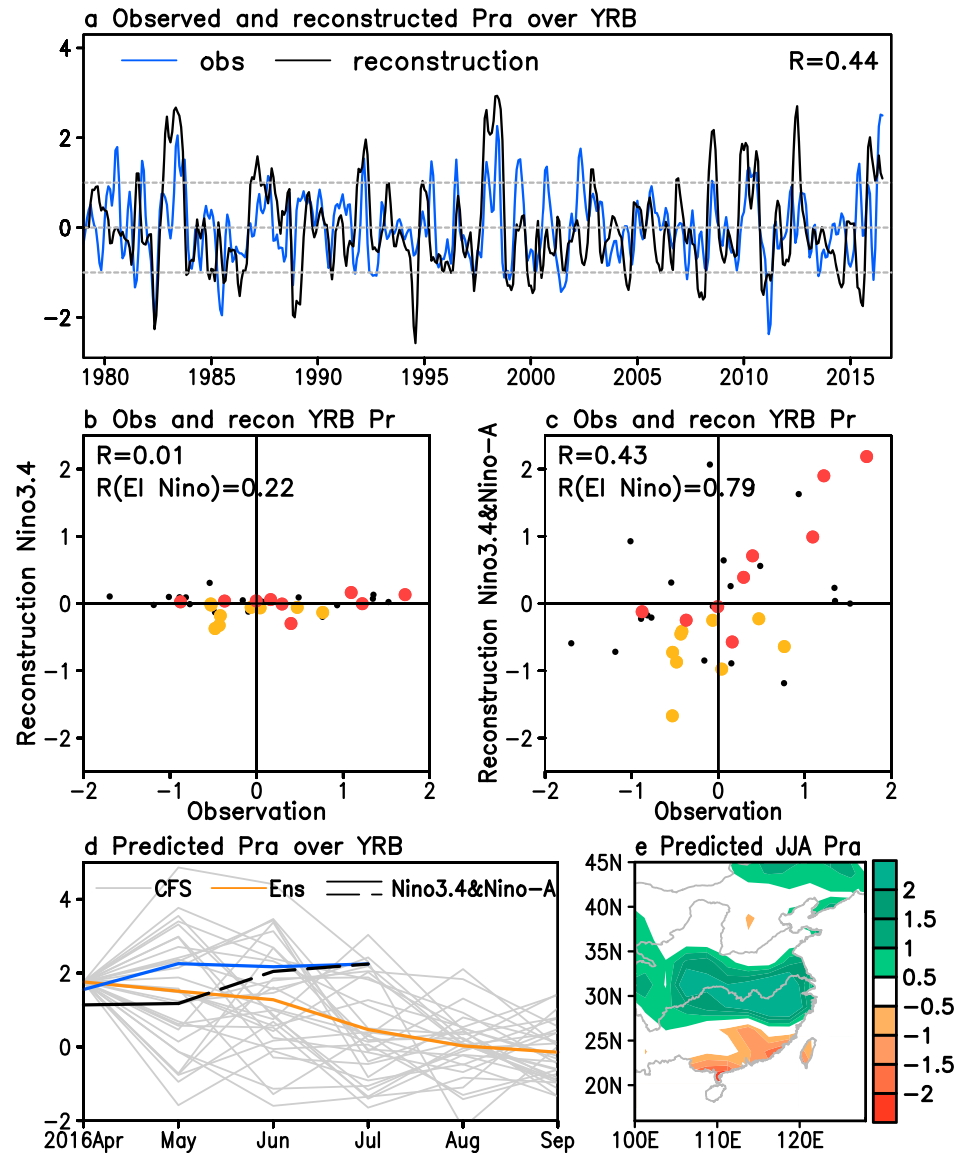


Figure 3. Yangtze River basin (YRB) precipitation reconstruction and prediction. (a) Normalized 3 month running mean of observed (blue line) and reconstructed (black line) YRB (area average over 110°E–120°E and 27°N–33°N) precipitation anomalies using Niño3.4 and Niño-A. (b and c) Relationship between observed and reconstructed JJA average YRB precipitation anomalies (mm/d) for the El Niño developing (yellow dots) and decaying summers (red dots), as well as for the remaining non El Niño JJA seasons (black dots). (d) Observed 2016 precipitation anomalies (blue line, mm/d), 3 month running mean reconstruction using Niño3.4 and Niño-A based on the observations (solid black line, mm/d) and forecast using Niño3.4 and Niño-A based on persistence (dashed black line, mm/d), as well as the individual CFSv2 member (grey lines, mm/d) and ensemble mean (orange line, mm/d) forecasts initialized in April 2016. (e) Persistence prediction using the Niño3.4 and Niño-A reconstruction for the JJA average precipitation anomalies in China (shading, mm/d).

partly due to larger impacts of weather noise on the off-equatorial SST anomalies. The potential predictability of ENSO complexity and the robust delineation of the ENSO/monsoon relationship suggest that observing and predicting ENSO’s dynamical evolution in the entire pantropical Pacific region will be very beneficial for better determining its impacts in densely populated areas such as the YRB.

4. Methods

The SST anomalies associated with ENSO’s complexity were examined based on the global sea ice and sea surface temperature analyses from the Hadley Centre (HadISST) provided by the Met Office [Rayner et al., 2003]. We

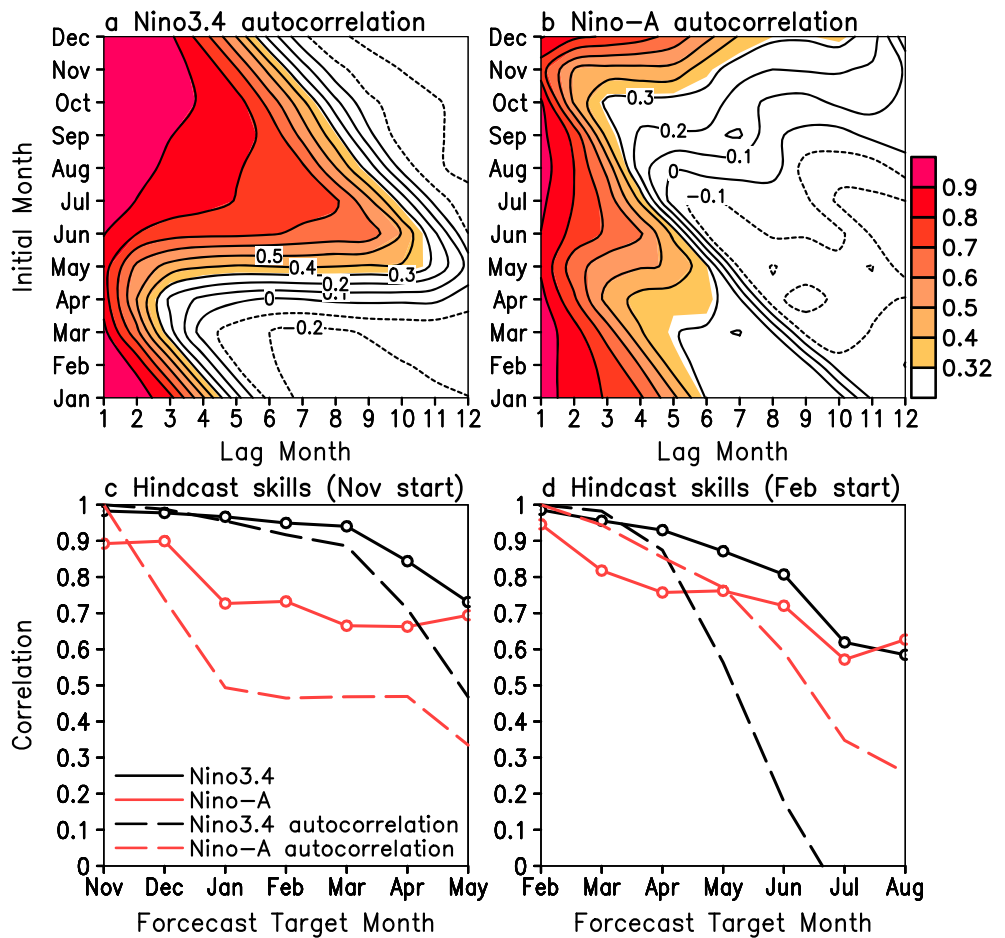


Figure 4. ENSO predictability. Autocorrelation (shading at the 95% confidence level) of (a) Niño3.4 and (b) Niño-A as a function of the starting month (ordinate) and lag month (abscissa). Niño3.4 and Niño-A hindcast skills in correlations (solid) based on two different starting months in (c) November and (d) February and corresponding autocorrelation (dashed). Hindcast data sets are from five dynamical models: The ENSEMBLES models from the UK Met Office (UKMO), Météo France (MF), the European Centre for Medium-Range Weather Forecasts (ECMWF), the Leibniz Institute of Marine Sciences at Kiel University (IFM-GEOMAR), and the Euro-Mediterranean Centre for Climate Change (CMCC-INGV).

utilized monthly 10 m wind data from European Centre for Medium-Range Weather Forecasts (ECMWF) ERA-Interim reanalysis [Dee et al., 2011] and the precipitation data from Climate Prediction Center Merged Analysis of Precipitation (CMAP) [Xie and Arkin, 1996], respectively. The seasonal forecasts of anomalous Yangtze River basin precipitation anomalies for the summer 2016 season (Figure 3d) are obtained from CFSv2 (32 ensemble members and ensemble mean) [Saha et al., 2014]. Our forecast and reconstructions (Figures 2b–2f and , 3b–2e and S7) are scaled by the ratio of the standard deviations of the observations and reconstructions.

All statistical significance tests were performed by using the two-tailed Student's *t* test. The effective degrees of freedom were determined by considering the autocorrelation of the respective time series, and statistical significance at the 95% confidence level is considered. To focus on the variability associated with ENSO (both interannual and combination mode near-annual variability), a 3–120 month band-pass filter is applied to each data set by using the second-order Butterworth filter to remove both decadal and subseasonal variabilities.

The ENSO C-mode was derived following the same approach as in Stuecker et al. [2013] as the second empirical orthogonal function mode of surface wind anomalies over the equatorial Pacific (10°S–10°N and 110°E–90°W). To demonstrate statistically that the PC2 wind forcing is the key driver for the SST pattern in Figure S1a, we use the normalized second principal component of the winds (PC2) as a forcing of a

conceptual thermodynamic SST anomaly (normalized T equation of the form: $dT/dt + \lambda T = \beta(PC2)_N$, where λ is a thermal damping coefficient ($1/30 \text{ day}^{-1}$) and β is a proportional constant ($1/60 \text{ day}^{-1}$)). The T regressed spatial pattern (Figure S1b) associated with the derived time series of T is almost the same as the pattern shown in Figure S1a (their spatial correlation reaches as high as 0.93 over the region from 40°E – 290°E and 40°S – 40°N)).

To illustrate that the Niño-A index captures both different ENSO flavors and their nonlinear interaction with the annual cycle, we decompose the subdecadal variability of the Niño-A index in terms of the theoretical C-mode index (CM_{SIMPLE}) and the El Niño Modoki (EMI) index based on the multiple linear regression method (for the period of 1979–2015) as follows:

$$\text{Niño} - A_N = 0.31*(CM_{\text{SIMPLE}})_N - 0.51*EMI_N. \quad (2)$$

Here CM_{SIMPLE} is the product obtained by the multiplication of the Niño3.4 index with the background annual cycle [Stuecker *et al.*, 2015a], and the subscript N denotes the use of normalized data. The Niño-A index exhibits the combined signals of CM_{SIMPLE} ($r=0.31$, 95% confidence level) and EMI ($r=-0.51$, 95% confidence level). The correlation between the reconstructed and observed Niño-A index reaches values as high as 0.66 (significant at the 95% confidence level).

Additional information about various SST anomaly indices [Saji *et al.*, 1999; Trenberth and Stepaniak, 2001; Ashok *et al.*, 2007; Xie *et al.*, 2009; Takahashi *et al.*, 2011; Wang *et al.*, 2013] and the supplementary figures can be found in the supporting information.

Acknowledgments

The data used to reproduce the results of this paper are available from the sources described in section 4. This study was supported by the China Meteorological Special Project (GYHY201506013), the National Nature Science Foundation of China (41675073), the U.S. National Science Foundation grant AGS-1406601, and the U.S. Department of Energy grant DE-SC000511.

References

- Ashok, K., S. K. Behera, S. A. Rao, H. Y. Weng, and T. Yamagata (2007), El Niño Modoki and its possible teleconnection, *J. Geophys. Res.*, *112*(C11), C11007, doi:10.1029/2006JC003798.
- Capotondi, A., et al. (2015), Understanding ENSO diversity, *Bull. Am. Meteorol. Soc.*, *96*, 921–938.
- Dee, D. P., et al. (2011), The ERA-Interim reanalysis: Configuration and performance of the data assimilation system, *Quart. J. Roy. Meteor. Soc.*, *137*, 553–597.
- Kao, H. Y., and J. Y. Yu (2009), Contrasting eastern-Pacific and central-Pacific types of ENSO, *J. Clim.*, *22*, 615–632.
- Klein, S. A., B. J. Soden, and N.-C. Lau (1999), Remote sea surface temperature variations during ENSO: Evidence for a tropical atmospheric bridge, *J. Clim.*, *12*, 917–932.
- Kug, J.-S., F.-F. Jin, and S.-I. An (2009), Two types of El Niño events: Cold tongue El Niño and warm pool El Niño, *J. Clim.*, *22*, 1499–1515.
- Latif, M., D. Anderson, T. Barnett, M. Cane, R. Kleeman, A. Leetmaa, J. O'Brien, A. Rosati, and E. Schneider (1998), A review of the predictability and prediction of ENSO, *J. Geophys. Res.*, *103*, 14,375–14,393, doi:10.1029/97JC03413.
- McGregor, S., A. Timmerman, N. Schneider, M. F. Stuecker, and M. H. England (2012), The effect of the South Pacific Convergence Zone on the termination of El Niño events and the meridional asymmetry of ENSO, *J. Clim.*, *25*, 5566–5586.
- McPhaden, M. J., S. E. Zebiak, and M. H. Glantz (2006), ENSO as an integrating concept in Earth science, *Science*, *314*, 1740–1745.
- Neelin, J. D., D. S. Battisti, A. C. Hirst, F.-F. Jin, Y. Wakata, T. Yamagata, and S. E. Zebiak (1998), ENSO theory, *J. Geophys. Res.*, *103*, 14,261–14,290, doi:10.1029/97JC03424.
- Rayner, N. A., D. E. Parker, E. B. Horton, C. K. Folland, L. V. Alexander, D. P. Rowell, E. C. Kent, and A. Kaplan (2003), Global analyses of sea surface temperature, sea ice, and night marine air temperature since the late nineteenth century, *J. Geophys. Res.*, *108*(D14), doi:10.1029/2002JD002670.
- Ren, H.-L., and F.-F. Jin (2011), Niño indices for two types of ENSO, *Geophys. Res. Lett.*, *38*, L04704, doi:10.1029/2010GL046031.
- Saha, S., et al. (2014), The NCEP Climate Forecast System Version 2, *J. Clim.*, *27*, 2185–2208.
- Saji, N. H., B. N. Goswami, P. N. Vinayachandran, and T. Yamagata (1999), A dipole in the tropical Indian Ocean, *Nature*, *401*, 360–363.
- Stuecker, M. F., A. Timmermann, F.-F. Jin, S. McGregor, and H.-L. Ren (2013), A combination mode of the annual cycle and the El Niño/Southern Oscillation, *Nature Geosci.*, *6*, 540–544.
- Stuecker, M. F., F.-F. Jin, A. Timmermann, and S. McGregor (2015a), Combination mode dynamics of the anomalous northwest Pacific anticyclone, *J. Clim.*, *28*, 1093–1111.
- Stuecker, M. F., F.-F. Jin, and A. Timmermann (2015b), El Niño-Southern Oscillation frequency cascade, *Proc. Natl. Acad. Sci.*, *112*, 13,490–13,495.
- Takahashi, K., A. Montecinos, K. Goubanova, and B. Dewitte (2011), ENSO regimes: Reinterpreting the canonical and Modoki El Niño, *Geophys. Res. Lett.*, *38*, L10704, doi:10.1029/2011GL047364.
- Tao, S. Y., and L. X. Chen (1987), A review of recent research on the east Asian summer monsoon in China, in *Review of Monsoon Meteorology*, edited by C. P. Chang and T. N. Krishnamurti, pp. 60–90, Oxford Univ. Press, New York.
- Trenberth, K. E., and D. P. Stepaniak (2001), Indices of El Niño Evolution, *J. Clim.*, *14*, 1697–1701.
- Trenberth, K. E., G. W. Branstator, D. Karoly, A. Kumar, N.-C. Lau, and C. Ropelewski (1998), Progress during TOGA in understanding and modeling global teleconnections associated with tropical sea surface temperature, *J. Geophys. Res.*, *103*, 14,291–14,324, doi:10.1029/97JC01444.
- Wallace, J. M., E. M. Rasmusson, T. P. Mitchell, V. E. Koussky, E. S. Sarachik, and H. von Storch (1998), On the structure and evolution of ENSO-related climate variability in the tropical Pacific: Lessons from TOGA, *J. Geophys. Res.*, *103*, 14,241–14,259, doi:10.1029/97JC02905.
- Wang, B., R. Wu, and X. Fu (2000), Pacific-East Asian teleconnection: How does ENSO affect East Asian Climate?, *J. Clim.*, *13*, 1517–1536.
- Wang, B., B. Xiang, and J.-Y. Lee (2013), Subtropical High predictability establishes a promising way for monsoon and tropical storm predictions, *Proc. Natl. Acad. Sci.*, *110*, 2718–2722.

- Webster, P. J., V. O. Magana, T. N. Plamer, J. Shukla, R. A. Tomas, M. Yanai, and T. Yasunari (1998), Monsoons: Processes, predictability, and the prospects for prediction, *J. Geophys. Res.*, *103*, 14,451–14,510, doi:10.1029/97JC02719.
- Weisheimer, A., F. J. Doblas-Reyes, T. N. Palmer, A. Alessandri, A. Arribas, M. Déqué, N. Keenlyside, M. MacVean, A. Navarra, and P. Rogel (2009), ENSEMBLES—A new multi-model ensemble for seasonal-to-annual predictions: Skill and progress beyond DEMETER in forecasting tropical Pacific SSTs, *Geophys. Res. Lett.*, *36*, L21711, doi:10.1029/2009GL040896.
- Xie, P., and P. A. Arkin (1996), Analyses of global monthly precipitation using gauge observations, satellite estimates, and numerical model predictions, *J. Clim.*, *9*, 840–858.
- Xie, S.-P., K. Hu, J. Hafner, H. Tokinaga, Y. Du, G. Huang, and T. Sampe (2009), Indian Ocean capacitor effect on Indo-Western Pacific climate during the summer following El Niño, *J. Clim.*, *22*, 730–747.
- Xie, S.-P., Y. Kosaka, Y. Du, K. Hu, J. S. Chowdary, and G. Huang (2016), Indo-Western Pacific Ocean capacitor and coherent climate anomalies in post-ENSO summer: A review, *Adv. Atmos. Sci.*, *33*, 411–432.
- Yang, J., Q. Liu, S. P. Xie, Z. Liu, and L. Wu (2007), Impact of the Indian Ocean SST basin mode on the Asian summer monsoon, *Geophys. Res. Lett.*, *34*, L02708, doi:10.1029/2006GL028571.
- Yeh, S.-W., J.-S. Kug, B. Dewitte, M.-H. Kwon, B. P. Kirtman, and F.-F. Jin (2009), El Niño in a changing climate, *Nature*, *461*, 511–514.
- Zhang, W., H. Li, M. F. Stuecker, F.-F. Jin, and A. G. Turner (2016), A new understanding of El Niño's impact over East Asia: Dominance of the ENSO combination mode, *J. Clim.*, *29*, 4347–4359.